Structural Elucidation of $Na_{2/3}NiO_2$, A Dynamically Stabilised Cathode Phase with Ni Charge- and Na Vacancy- Ordering.

James M. A. Steele,[1, 2] Annalena R. Genreith-Schriever,[1] Joshua D. Bocarsly,[3] Liam A. V. Nagle-Cocco,[2,4] Farheen N. Sayed,[1] Marie Juramy,[1] Christopher A. O'Keefe,[1] Fabio Orlandi,[5] Pascal Manuel,[5] Siân E. Dutton [2 *] & Clare P. Grey [1 *]

[1] Yusuf Hamied Department of Chemistry, University of Cambridge, Cambridge, CB2 1EW, UK

[2] Cavendish Laboratory, University of Cambridge, JJ Thomson Avenue, Cambridge, CB3 0HE, UK

[3] Department of Chemistry and Texas Center for Superconductivity, University of Houston, Houston, TX 77004, USA

[4] Current address: Stanford Synchrotron Radiation Lightsource, SLAC National Accelerator Laboratory, Menlo Park, CA 94025, USA

[5] ISIS Facility, Rutherford Appleton Laboratory, Harwell Campus, Didcot OX11 0QX, UK

[*] Email: sed33@cam.ac.uk, cpg27@cam.ac.uk

Abstract:

$NaNiO_2$ (NNO) has been investigated as a promising sodium-ion battery (NIB) cathode material, but it is limited by degradation-induced capacity fade. On desodiation, NNO forms multiple phases with large superstructures due in part to Na^+-ion vacancy ordering, however, their structures are unknown. Here, we report a structural solution to the $Na_{2/3}NiO_2$ ($P^{/}3$) de-sodiated phase using combined Rietveld refinement of high-resolution synchrotron X-ray (SXRD) and neutron diffraction (NPD) data, magnetic susceptibility, and ^{23}Na solid-state nuclear magnetic resonance (ssNMR) spectroscopy. Our experimental results are compared to *Ab Initio* Molecular Dynamics (AIMD) simulations, which indicate multiple low-energy structures that are dynamically populated. We observe a combination of competing effects which contribute to the resultant dynamic nature of the structure, including honeycomb ordering of mixed-valence Ni, orbital-ordering of Jahn-Teller (JT) distorted Ni^{3+}, and zigzag Na^+/vacancy ordering. Our work provides evidence of the multiple contributions to the structures of de-sodiated $Na_{2/3}NiO_2$, along with a framework for investigating the other unsolved de-sodiated structures. This work may also inform understanding of the Jahn-Teller evolution in other nickel-rich lithium and sodium ion cathodes, such as $LiNiO_2$.

Graphical Abstract:

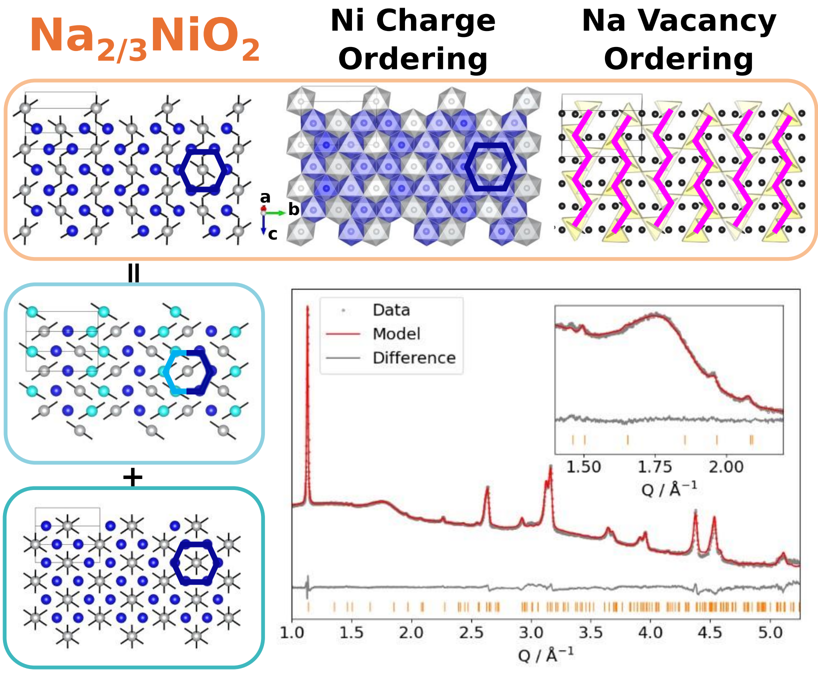

Introduction:

Na ion batteries (NIBs) are well suited to large-scale, low-cost applications. Na is relatively uniformly distributed across the globe, being more than 1000 times more abundant than Li in the Earth's crust (23,000 ppm vs 20 ppm).[1] However, Na is larger and heavier than Li, meaning volumetric/specific capacities (charge per unit volume/mass respectively), of NIBs are inherently lower than for equivalent LIB cathodes (*i.e.* $NaNiO_2$ *vs* $LiNiO_2$). Therefore, optimizing the performance, stability, and reversibility of Na-ion batteries is an important research objective.

Ni-rich cathodes for both Na and Li-ion batteries are the subject of intensive research efforts, with the aim of increasing energy density, whilst decreasing reliance on expensive and ethically dubious cobalt.[2,3] For Li-ion batteries, the parent compound $LiNiO_2$ has a structure which remains controversial due to open questions about the nature of the Jahn-Teller (JT) distorted d^7 Ni^{3+} cations and possible co-operative JT ordering.[4–8] The average crystal structure reported from combined refinement of synchrotron x-ray (SXRD) and neutron powder diffraction (NPD) data is rhombohedral ($R\bar{3}m$), containing no bulk cooperative JT distortion.[9,10] Computational and experimental studies have put forward evidence of both order-disorder and displacive models for the JT transition.[11,12] A complete description of the structure is complicated further by the presence of anti-site defects and off-stoichiometry (primarily lithium deficiency), which are difficult to control reproducibly in the synthesis of this material.[13,14] The complexity of the parent $LiNiO_2$ phase adds further complexity to the understanding of the phases that form upon electrochemical cycling, hindering efforts to rationally improve performance.

By contrast to $LiNiO_2$, the pristine Na-analogue parent compound ($NaNiO_2$) is in many ways a simpler system as the greater size of the Na^+ cation prevents the formation of anti-site defects, improving reproducibility between synthesised materials, and facilitating consistent structural and electrochemical properties.[15] Furthermore, the Na^+ cation contributes to increased volume changes, and a range of stable, de-sodiated ($Na_{1-x}NiO_2$) phases are observed during cycling.[15–17] At room temperature, colinear cooperative ordering of JT-distorted octahedra in $NaNiO_2$ results in a monoclinic ($C2/m$) structure termed $O^{/}3$, as opposed to the rhombohedral O3 unit cell of the non-JT analogue compounds (*e.g.,* $NaCrO_2$ [Cr^{3+},d^3], $NaCoO_2$ [Co^{3+}, d^6]) (SI-1). Here the terminology O3 denotes octahedral (O) coordination of the Na^+ ions, with three TMO_2 slab layers required to describe the stacking of the unit cell, as per Delmas' naming convention.[18] Similarly, P would denote a prismatic alkali-ion coordination. Distortion from ideal O/P phases is denoted by a prime marker ($^{/}$), with the number of markers increasing for each new phase in the order of reporting. On heating, $NaNiO_2$ undergoes a reversible first-order displacive Jahn-Teller phase transition between 465-495 K, resulting in an O3 phase that is isostructural with the Cr/Co analogues, and with $LiNiO_2$.[19,20]

Sodium-ion battery (NIB) cathodes, in general, are known to exhibit stable phases throughout their voltage profiles with ordered arrangements of sodium ions (Na_{Na}^{x}) and sodium ion vacancies ($V_{Na}^{/}$). For example, in $Na_{1-x}CoO_2$, at least two ordered phases are observed (*i.e.* $Na_{2/3}CoO_2$ and $Na_{1/2}CoO_2$).[21,22] Similarly, the voltage profile of $NaNiO_2$ presents a range of characteristic biphasic phase transitions as a function of Na content (Na_xNiO_2; x ~ 1, 2/3, 1/2, 2/5, 1/3, 0.91), spanning both octahedral and prismatic Na coordination environments.[23,24] Resulting in the overall transformation of $O^{/}3$ (Na_1) -> $P^{/}3$ ($Na_{2/3}$) -> $P^{//}3$ ($Na_{1/2}$) -> $O^{//}3$ ($Na_{2/5}$) -> $O^{///}3$ ($Na_{1/3}$). The system returns to $O^{////}3$ ($Na_{\sim 0.91}$) at the end of discharge, as it does not appear to be possible to fully re-sodiate via electrochemical methods.[15,16,25] The origins of this complex phase evolution are not well understood, but could be expected to be related to the interplay of JT distortions of the d^7 (t_{2g}^6, e_g^1) Ni^{3+} ions and Na vacancy and Ni charge ordering. Understanding the structural evolution of Na_xNiO_2 provides an excellent opportunity to study the role of charge, orbital, and vacancy ordering in Ni-rich cathode materials.

Solutions for the structures of the de-sodiated Na_xNiO_2 phases have not been reported, though pattern indexing of XRD data identified lattice parameters and possible space groups for each phase.[15,16,23,25] Based on these, O/P phases were assigned through cell parameters, as prismatic unit cells typically have greater β-(monoclinic) angle than octahedral phases (typically ~120 ° vs ~110 °). De Boisse identified small superstructure diffraction peaks, and determined supercell space groups and lattice parameters (but not atom positions) from synchrotron x-ray diffraction data as a function of the parent O$^{/}$3 lattice parameters (cell$_{O'3}$) for $NaNiO_2$ [space group = C2/m, $a_{O'3}$ = 4.970 Å, $b_{O'3}$ = 2.862 Å, $c_{O'3}$ = 5.742 Å]): P$^{/}$3 ($Na_{2/3}NiO_2$) = P2$_1$/a [$a_{O'3}$*3$b_{O'3}$*$c_{O'3}$], P$^{//}$3 ($Na_{1/2}NiO_2$) = P2$_1$/m [$a_{O'3}$*2$b_{O'3}$*$c_{O'3}$], O$^{//}$3 ($Na_{2/5}NiO_2$) = C2/m [$a_{O'3}$*5$b_{O'3}$*$c_{O'3}$].[26] A structure for the P$^{/}$3 phase was presented in a density functional theory (DFT) and experimental study of $Na_{2/3}MnO_2$, which focussed on calculations. However, the reported structure obtained after Rietveld refinement of in-situ SXRD data results in unphysical Ni-O and Na-O bond lengths.[27]

Here we report a structure for the first de-sodiated phase of NNO, P$^{/}$3 $Na_{2/3}NiO_2$, prepared electrochemically. Our structure is consistent with previous studies of the lattice parameters and symmetry,[26,27] but by using a combined refinement of high-resolution SXRD and NPD data, we are now able to elucidate a complete structural model. We observe both Ni charge and Na vacancy ordering in honeycomb and zigzag arrangements respectively. Two crystallographically distinct Ni sites are observed, present in a 2:1 ratio and with clear signs of charge disproportionation. Our model is consistent with magnetic susceptibility and solid-state ^{23}Na NMR measurements, which further demonstrate that the proposed model additionally describes the local structure. From *Ab-Initio* Molecular Dynamics (AIMD) simulations, we find multiple low-lying structures, all of which have Ni charge and Na vacancy ordering, revealing the dynamic nature of the system.

Experimental/Methods:

$NaNiO_2$ Synthesis

$NaNiO_2$ was synthesised *via* a solid-state route. All reactant powders (NiO *Alfa Aesar Puratronic® 99.998 %*, Na_2O_2 *Sigma 97%*) were mixed and ground manually using an agate pestle and mortar for 15 minutes within an Ar-filled glovebox, before being pelletised using a pellet press at approximately 5 MPa, then transferred to an alumina crucible. All syntheses were carried out at 700 °C (ramp rate = 3 °C min^{-1}, cooling ramp rate set to 10 °C min^{-1} resulting in cooling at ambient rate in the absence of active cooling) for 10 hours, under continuous O_2 flow at a rate of approximately 30 ml min^{-1}. Air/moisture exposure was minimised through rapid transfer of the product from the furnace to an Ar filled glovebox, though it was not possible to eliminate exposure completely.

Cell Fabrication, Electrochemical Cycling, and *Ex situ* Sample Preparation

In order to prepare large sample quantities of the de-sodiated phase suitable for NPD, we used 1" diameter Swagelok cells. The synthesised active cathode material ($NaNiO_2$) and conductive carbon (Super P) were mixed in a 70:30 ratio for ~15 minutes using an agate pestle and mortar, then the resultant powder was added directly to the Swagelok stainless steel current collector. The cells were assembled in the following order, starting from: the stainless steel plunger, stainless steel current collector, cathode/carbon mixture, 2 x 1 " fibre glass spacer, 400 µL electrolyte (1M $NaPF_6$ in propylene carbonate [PC], produced as required to minimise degradation), 15/16" Na metal anode, stainless steel current collector, a rigid spring, stainless steel plunger. The body of the cell was wrapped with Kapton film internally to prevent short-circuiting/degradation. See Figure S2 for more information. The Na metal anodes were produced at the time of use as follows: since the Na metal is stored in mineral oil, the oil was first washed off in a glass vial using heptane, before the metal is rolled to a suitable thickness, and punched manually with a 15/16" manual punch.

Swagelok cells were cycled using a BioLogic potentiostat, controlled by EC-Lab software, in a temperature-controlled room (at 25 °C), using a charge rate of C/100, preceded by a voltage hold at 2.9 V for 48 h to aid in complete conversion to the desired phase.

Following electrochemical cycling, samples were retrieved by disassembling the Swagelok cells, and scraping the electrode powder from the current collector, into a glass jar, and washing with dimethyl carbonate (DMC). The cathode powders were allowed to settle before the DMC (containing any remaining electrolyte and salt) was removed *via* syringe, with any remaining DMC being evaporated under dynamic vacuum of -1 bar (relative pressure) for 2 hours. All disassembly and washing was carried out in an Ar-filled glovebox.

All samples were stored in sealed glass vials in an Ar filled glovebox, until required for measurement, to prevent exposure to air/moisture.

Powder X-ray Diffraction

SXRD experiments were carried out at beamline I-11 at Diamond Light Source, UK.[28] All capillary samples were transferred to 0.5 mm diameter borosilicate glass capillaries, sealed with epoxy glue, within an argon filled glovebox to prevent air/moisture exposure. The samples were measured using the Multi-analyser Crystal (MAC) detectors, or Position Sensitive Detectors (PSD) as indicated in the text, at energies/wavelengths of 15 keV (λ = 0.827 Å) as refined against a Si standard. Measurements using the MAC detectors were collected at a step-size of 0.001 °, and processed through re-binning at 0.010 °. All reported measurements were collected at room temperature (approximately 25 °C).

Neutron Powder Diffraction

Neutron Bragg diffraction measurements were obtained using the WISH diffractometer at the ISIS Neutron and Muon Source, UK, which provides very high signal-to-noise in the region where superstructure peaks are expected.[29] Within a helium filled glovebox, samples were loaded into 5 mm internal diameter vanadium cans, sealed with indium wire to prevent air/moisture exposure. The cans were loaded onto a sample changer, which was placed within the instrument sample tank under vacuum. Data were collected across all 5 pairs of instrumental banks (average 2θ of bank pairs 1_10 = 27.0 °, 2_9 = 58.33 °, 3_8 = 90.00 °, 4_7 = 121.66 °, 5_6 = 152.82 °), on the sample containing ~ 100 mg of $Na_{2/3}NiO_2$, and ~43 mg of carbon (the cathode mixture), for approximately 4 hours to ensure suitable signal-to-noise ratio for distinguishing the observed superstructure peaks. All reported measurements were collected at room temperature (approximately 25 °C).

ISODISTORT + TOPAS Academic Superstructure refinements

Rietveld and Pawley refinement of XRD/NPD data were carried out using TOPAS-Academic,[30–32] with additional input from ISODISTORT as referred to in the discussions section.[33,34] For combined refinement of SXRD/NPD data, the data were weighted such that the total contributions of the one XRD pattern and five NPD patterns, collected across the WISH instrument's 10 (five mirrored sets of two) banks were equal.[29]

The XRD pattern background was fit with a Chebyshev polynomial with 38 terms. XRD peak shapes contributions from the beam were accounted for using a Thompson-Cox-Hastings pseudo-Voigt peak shape, the parameters of which were refined against a measured Si standard.[35] Sample contributions to peak shapes were modelled using Lorentzian and Gaussian crystallite size parameters, and Stephens monoclinic strain broadening.[36]

The complex nature of the NPD pattern backgrounds necessitated the use of a user defined background using the bkg_file() macro in TOPAS-Academic. The background was generated using the automated background function in the WinPLOTR application in the Fullprof software suite,[37,38] followed by interpolation of these peaks using Python. Instrumental contributions to peak shapes (DIFC, DIFA, ZERO, and tauf_1) in the NPD data were first fit to a measured NaCAlF standard. DIFC, initially 0.0, was later allowed to refine for all but the highest resolution bank, allowing for small differences in sample position within the instrument, the ZERO (which accounts for timing signal differences and finite response times in electrical components of the instrument) and tauf_1 (used in the moderator correction) were kept constant.[39] These instrumental parameters were incorporated into TOF Lorentzian and Gaussian crystallite size and strain parameters, in addition to a TOF_2FP_Voigt peak shape.

Magic angle spinning solid state NMR

Samples were packed into 1.3 mm diameter ZrO_2 magic angle spinning (MAS) rotors, in an argon filled glovebox. The rotors were additionally packed with Teflon tape due to low sample quantity. ^{23}Na spectra were measured using either a Bruker Biospin Solid-State AV500 (500 MHz, 11.7 T) with 60 kHz MAS and a, "H13708 MASDVT500W2 BL1.3 N-P/F-H" probe, or a Bruker AVANCE NEO (400 MHz, 9.4 T) spectrometer, with a "1.3 mm LTMAS H/FXY" probe. ^{23}Na spectra were referenced to NaCl as an external reference at 0.0 ppm. Experiments were optimised to enable direct excitation of ^{23}Na nuclei (pulse length = $\pi/4$), utilising Hahn-echo and pj-MATPASS pulse sequences.[40–42] For variable temperature measurements, stated values are those of the sample, estimated based on the known relationship between the spin lattice relaxation time (T_1) and temperature in ^{79}KBr (measured in a separate experiment), with intermediate points based on the empirical relationship between measured temperature and temperature calculated at set points.[43]

Magnetic Measurements

Magnetic property measurements were performed using a Quantum Design Magnetic Property Measurement System (MPMS3). Within an argon filled glovebox, the sample of 26.9 mg total mass, (18.8 mg active cathode mass) was wrapped in polyethylene film and loaded into polypropylene powder sample capsules. The sample holders were then mounted into a brass sample holder and measured in vibrating sample magnetometer mode.

DC magnetic susceptibility measurements χ(T) = dM/dH were performed on an *ex situ* sample. In order to study the magnetic behaviour and possible magnetic ordering at low temperature, susceptibility as a function of temperature (on heating) was collected under both zero field cooled (and ZFC) and field cooled (FC) conditions at between 1.8 K and 300 K under constant external field of 100 Oe. Additionally, FC data between 1.8 K and 350 K was collected under a field of 20 kOe.

At all fields, the magnetic susceptibility is in the low field limit where $\chi(T)$ = dM/d$H \approx M/H$, and the $\chi(T)$ measured at 20 kOe was fit between 175 K and 350 K using the Curie-Weiss law:

$$\chi(T) = \frac{C}{T - \theta} + \chi_0$$

Where C is the Curie constant, θ is the Weiss temperature, and χ_0 is a temperature-independent susceptibility term that accounts for constant diamagnetic or paramagnetic contributions to the signal (which may arise from the sample itself, or from the sample holder or electrode additives).

Magnetic susceptibility was also measured as a function of magnetic field strength between 70 kOe and –70kOe at temperatures of 1.8 K, 11 K, 18 K, 50 K, and 100 K (SI9c).

DFT, AIMD, and NMR Shift Calculations

AIMD simulations were performed according to the Generalized Gradient Approximation (GGA) proposed by Perdew, Burke, and Ernzerhof,[44] and the projector augmented wave method (PAW),[45] as implemented in the Vienna Ab Initio Simulation Package (VASP).[46,47] The plane-wave energy cutoff was set to 500 eV and a 2 x 2 x 2 Monkhorst-Pack k-point grid was used.[48] Simulations at varying temperatures were performed with the unit cell comprising 22 ions and checked against calculations with a 2 ~$a_{O'3}$ x 6 ~$b_{O'3}$ x 2 ~$c_{O'3}$ supercell comprising 176 ions, yielding nearly identical van Vleck plots of the Q_2,Q_3 ordering parameters. The convergence criteria for the electronic and ionic relaxations were set to 10^{-6} eV and $5\cdot10^{-3}$ eV/Å, respectively.

For Ni, the $4s^2 3d^8$ electrons were treated as valence electrons. To account for the strongly correlated d electrons, a rotationally invariant Hubbard U parameter of U_{eff} = 6 eV was selected, which was used successfully in previous studies of layered oxide cathodes including the pristine parent material $NaNiO_2$.[49,4,5,20] For oxygen, the $2s^2 2p^4$ electrons were considered in the valence.

AIMD simulations were performed for the isothermal-isobaric ensemble *(NpT*, constant pressure, particle number, and temperature) at zero pressure. A Langevin thermostat was used with friction coefficients set to 10 ps^{-1}.

The relative stability of the different structures and the Fermi contact shifts were calculated based on DFT calculations with the all-electron CRYSTAL software package using the hybrid functional B3LYP with 20% Fock exchange.[50] The basis sets proposed by Oliveira and Bredow were used, on supercells comprising 22 ions.[51] Geometry optimisations were performed until the energies differed by no more than 10^{-6} eV and forces no more than 0.001 eV/Å. A Monkhorst-Pack k-point grid of 4x4x4 was chosen for the geometry optimisations. Single-point calculations of the energies and the spin density at the nucleus, decisive for the Fermi contact shift, were performed with a finer k-point grid of 6x6x6 k-points.

Effective magnetic moments were obtained using the default CRYSTAL projection of the spin densities onto atomic sites. The hyperfine coupling constant and Fermi contact shift were calculated from the nuclear spin density according to Kim *et al.*,[52] and scaled to 320 K (while the experiment was nominally conducted at room temperature, frictional heating of the rotor results in a sample temperature of ca. 320 K) using the Curie-Weiss parameters reported in this work.

The van Vleck mode analysis of the AIMD snapshot cells was carried out using the Python-based VanVleckCalculator software.[53] Code is available on GitHub.[54]

Results:

Synthesis of the $P^{/}3$ Phase

The pristine active cathode material ($NaNiO_2$, $O^{/}3$) was synthesised as described in Methods, with identity and phase purity confirmed by Rietveld refinement of the literature reported structure against SXRD data (SI-3). Prior to electrochemical synthesis of the $P^{/}3$ phase, complete charge-discharge cycles were measured showing the expected behaviour and allowing for selection of the appropriate voltage (2.9 V for $Na_{2/3}NiO_2$, $P^{/}3$) to isolate phase pure samples (Figure S4a-b).[15] Because of concerns of reversibility, the samples were always prepared on fresh electrodes, i.e., during the first charge. The phase purity of ex-situ samples was confirmed by XRD/NPD (Figures S5a-d & S6a-b).

Structure of P$^{/}$3 Phase ($Na_{2/3}NiO_2$)

From SXRD the P$^{/}$3 was found to be phase pure (Figure S5c) and, in agreement with literature, superstructure peaks were observed in the range of 1.40 – 2.20 Å^{-1} (Figures 1a-b).[26] NPD collected on the WISH diffractometer shows superstructure peaks in the same Q range (Figure S6b). All observed superstructure peaks in both datasets could be indexed to a cell consistent with previously reported space group ($P2_1/c$) and lattice parameters (a = 4.972 Å, b = 8.589 Å, c = 5.739 Å, β = 105.84 $^{\circ}$) (SI6a-d) consistent with the previous report[26].

ISODISTORT was used to produce candidate structural models for the P$^{/}$3 structure.[34] As the fully sodiated (O$^{/}$3) phase has octahedrally coordinated Na ions, we started with a hypothetical parent P$^{/}$3 structure (ST1) with no superstructure ordering. The lattice parameters of this P$^{/}$3 parent cell were set to values refined by fitting the SXRD pattern, ignoring the superstructure peaks. ISODISTORT was then used to generate possible 1x3x1 superstructures (k point: 0, 1/3, 0) with space groups that would be consistent with the observed superstructure peaks. Of these candidate structures, the best fit was found using a structure with space group $P2_1/c$ (irreducible representation LD2 k2t2, with order parameter direction P1) (S-4). By comparison to the original (O$^{/}$3, C2/m), and hypothetical (P$^{/}$3, C2/m) which contain single Na, Ni, and O sites, the lower symmetry structure (P$^{/}$3, $P2_1/c$) with $\sim a_{O'3}$*3$\sim b_{O'3}$*$\sim c_{O'3}$, (approximate due refinement of lattice parameters in hypothetical parent to SXRD data) contains: 2 Ni sites ($Ni_{(1)}$ = 2a, $Ni_{(2)}$ = 4e) generating honeycomb ordering, 3 possible Na sites (all 4e), which would be expected to have 1/3 occupancy each if all occupied, and 3 O sites (all 4e), allowing for Ni orbital (JT), charge, and Na vacancy ordering. Refinement of Na site occupancies indicates that a single Na ($Na_{(3)}$ 4e) site is fully occupied, with the other sites ($Na_{(1)}$, $Na_{(2)}$) vacant, giving a composition of $Na_{2/3}NiO_2$, consistent with literature reports and our electrochemistry (SI3a-b).[16,25] In subsequent refinements the occupancies of the $Na_{(3)}$ and $Na_{(1/2)}$ sites (4e) were fixed to 1 and 0 respectively. Further refinement of the allowed atomic coordinates for Ni and O and the occupied $Na_{(3)}$ site enable a good fit to the data, with all superstructure peaks fit well in both the SXRD and neutron diffraction (R_{wp} = 1.473).

In the refined structure, we find large isothermal (B_{iso}) parameters for the $O_{(2)}$ and $Na_{(3)}$ sites, with all other thermal parameters refining to 0.498-1.155 Å^2. Adding anisotropic displacement parameters (ADPs) for the $O_{(2)}$ site results in a large, thin displacement ellipsoid along the direction of the $Ni_{(1)}$-$O_{(2)}$ bond, suggesting significant vibrations or disorder along the JT axes. Alternatively, we can model the $O_{(2)}$ using a split site model with one long and one short $Ni_{(1)}$-$O_{(2)}$ bond which refine to 2.172(24) Å and 1.914(26) Å respectively. When we model the $Na_{(3)}$ site with anisotropic thermal parameters, these manifest as ellipsoids pointing directly through the large prismatic faces of the prismatically coordinated Na, directly into a vacancy (known to be a facile pathway for Na mobility).[55] The refined structure is displayed in Figures 2a-f (full structural details presented in ST3).

Our structural model contains edge-sharing triangular prisms occupied by Na^+ ions (termed "herringbone" patterning by Wang *et al.* but more widely referred to as "zigzag"*)*,[56] and a honeycomb ordering of the Ni sites, with the occupied Na sites broadly correlated with the more contracted $Ni_{(2)}O_6$ octahedra in adjacent layers (Figures 2e-f). The two Ni sites have dramatically different bond lengths with average Ni-O bond lengths for the honeycomb $Ni_{(1)}$ and $Ni_{(2)}$ sites of 1.985(15) Å and 1.93(8) Å respectively. This suggests that the two Ni sites have different ionic charges with the $Ni_{(1)}$ sites having a lower oxidation state relative to $Ni_{(2)}$. We note that Ni-O bonds in nickelates are known to have covalent character, *i.e.* charge ordering is expected to be reflected both in the Ni and O lattices. For the sake of clarity, we will refer to charges in terms of formal ionic charges (assuming ionic bonds) as the formal charges directly correlate with the Ni spin states. The bond valence sum (BVS) method was used to calculate the nominal charge of the two Ni sites. We considered a range of ideal bond length

(R_0) values, finding that the most suitable was Ni^{4+}-O^{2-} ($R_{0,Ni4+}$ = 1.734 Å, $B_{0,Ni4+}$ = 0.335 Å). We suspect that this is due to the non-uniform Ni-O bond length distribution caused by JT effects (See S-6 for more information). We obtain values of $Ni^{3.07+}$ and $Ni^{3.43+}$ for $Ni_{(1)}$ and $Ni_{(2)}$, respectively, giving an average charge of $Ni^{3.31+}$. This is close to the expected value of $Ni^{3.33+}$ for $Na_{2/3}NiO_2$.

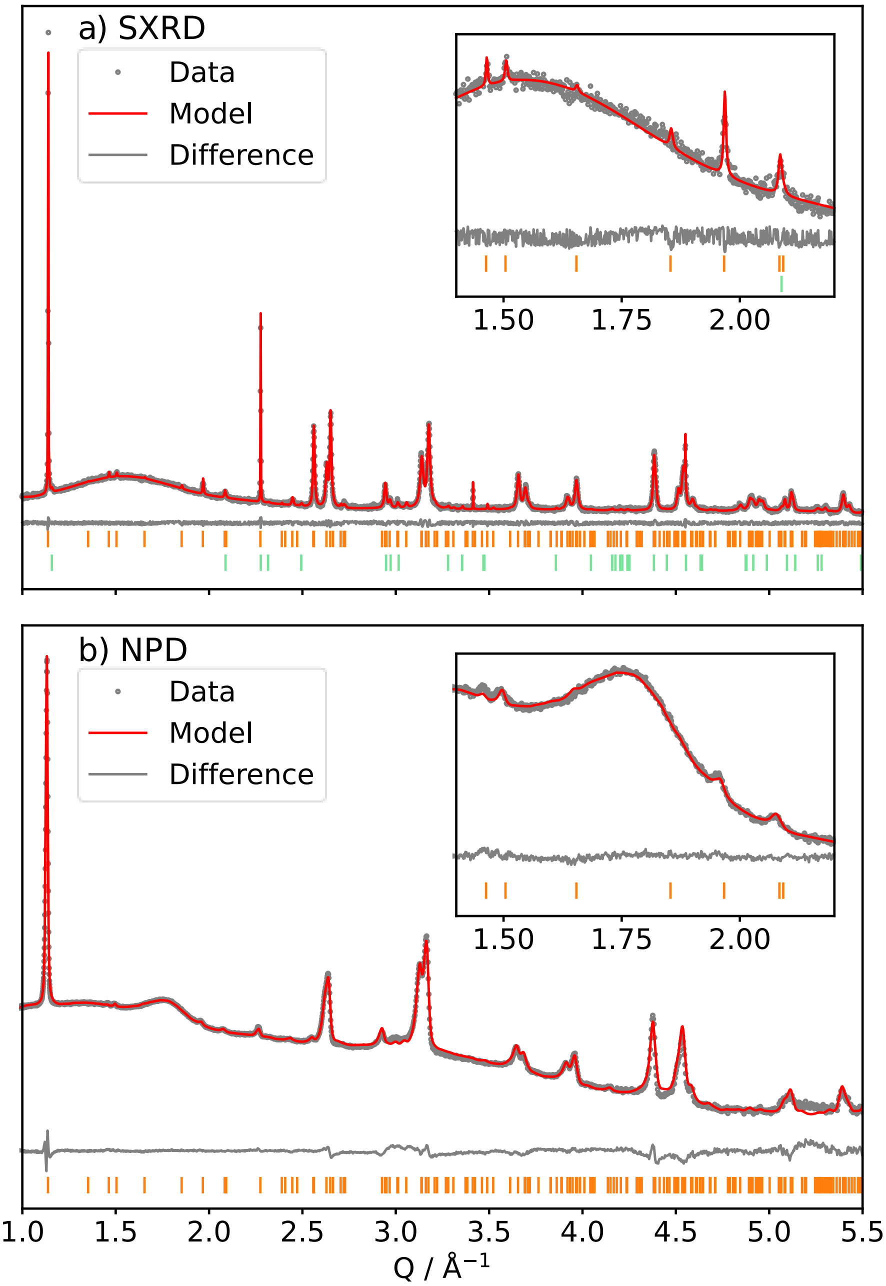

Figure 1: a) Combined refinement of a) SXRD and b) NPD (average 2θ of bank pairs 58.33 °). Tick marks are displayed below for P′3 (orange) and O′′′′3 minor impurity (green) in the SXRD sample. Data collected at room temperature (approximately 25 °C). The square root of intensity is plotted on the y-axis for visual clarity. Insets show the superstructure peak region.

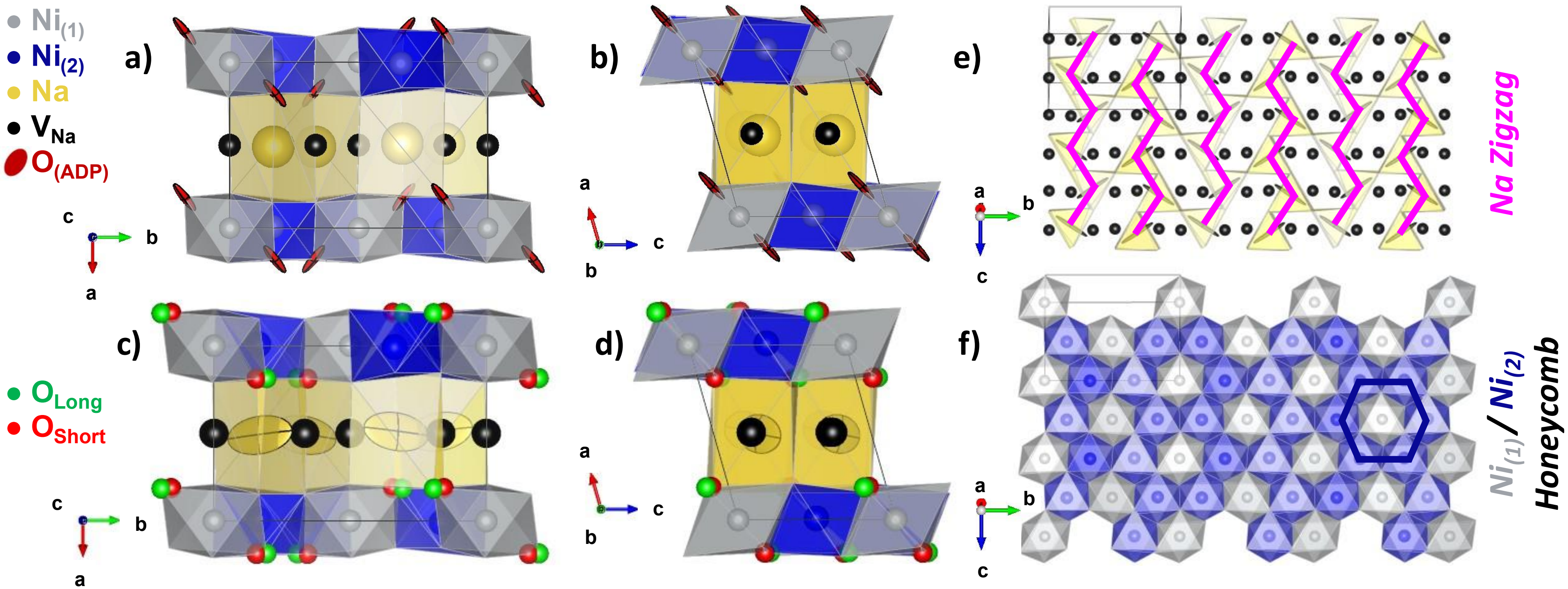

Figure 2: Structural model for P/3 phase as determined from combined refinement of SXRD and NPD data. The structural model with anisotropic ADPs for the $O_{(3)}$ site is shown along the a) c, and b) b directions. The structural model with anisotropic ADPs for the $Na_{(1)}$ site, and split $O_{(3)}$-site is shown along the c) c, and b) b directions. e) Na/Vacancy zigzag ordering of edge-sharing occupied Na trigonal prismatic sites (in yellow) in the Na-layer (pink zigzags overlayed for visual clarity to show the repeating zigzag motif). f) Honeycomb ordering of the two Ni sites on the triangular Ni lattice. In c/f the unit cell (black box outline).

^{23}Na ssNMR

Variable-temperature ^{23}Na solid state magic angle spinning NMR (MAS ssNMR) of ^{23}Na was performed on the P$^{/}$3 phase (Figure 3a-b). A broad, high-frequency resonance, with a series of spinning sidebands, is observed in the Hahn Echo experiment (Figure 3a). The peaks shift further to higher frequencies, with decreasing temperature. The large shift is ascribed to a hyperfine (Fermi contact) interaction between the ^{23}Na nuclei and the unpaired electrons on the Ni^{3+} ions,[57] the increased shift with decreasing temperature resulting from an increase in magnetic susceptibility (strictly, the time-averaged value of the magnetic moment) with temperature.[58] A broadening of the spinning sideband manifold seen on cooling can similarly be ascribed to the increase in magnetic susceptibility, in possible combination with decreasing Na^+-ion mobility (this is currently under investigation, but beyond the scope of the present work). We also observe a resonance at ~0 ppm, which we attribute to diamagnetic impurities such as NaF, $NaHCO_3$ and Na_2CO_3 from the as-synthesised material and from degradation of propylene carbonate electrolyte.

In the pj-MATPASS experiments – used to separate the isotropic resonance from its spinning sidebands (Figure 3b) - we observe a single isotropic paramagnetic resonance from the P$^{/}$3 phase at room temperature (~1086 ppm at 290 K), down to the lowest measured temperature (~2650 ppm at 122 K). This is consistent with the single Na environment in the vacancy ordered structure refined from SXRD and NPD data. This resonance is observed at a noticeably lower shift in comparison to that previously reported for the pristine O$^{/}$3 $NaNiO_2$ material (~1086 ppm vs 1460 ppm; for comparison of P$^{/}$3 and O$^{/}$3 see Figure S5e).[20] We ascribe this to the decreased hyperfine shift, resulting from the oxidation of a 1/3 of the Ni^{3+} in the $Na_{2/3}NiO_2$ phase to diamagnetic Ni^{4+} ions.

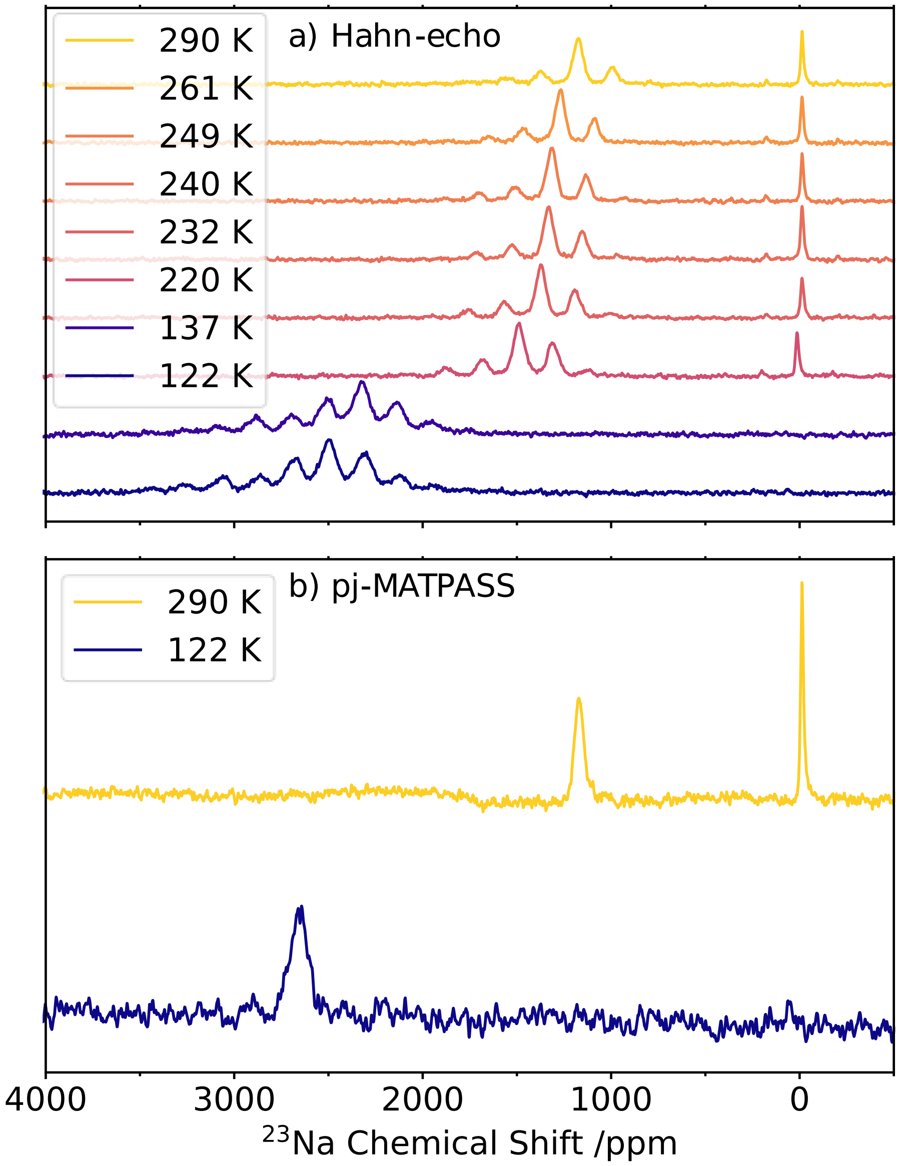

Figure 3: Variable temperature ^{23}Na MAS ssNMR: a) Hahn-echo and b) pj-MATPASS spectra of the de-sodiated P$^{/}$3 phase, acquired from 122 K – 290 K with 20 kHz MAS. Measured (400 MHz, 9.4 T) field strength. The offset frequency was moved with temperature to optimise the signal intensity of the higher frequency resonance; the ~0 ppm diamagnetic peak was consequently no longer observed at low temperatures at the offset frequencies shown in these spectra.

Magnetic Susceptibility and Curie-Weiss Fitting

The magnetic susceptibility of the $P^{/}3$ phase shows paramagnetic behaviour at high temperatures, $T >$ 100 K. On further cooling the ZFC and FC susceptibility diverge, and a cusp in the ZFC susceptibility is observed at $T \approx 25$ K. The low temperature magnetic properties are tentatively ascribed to either long range magnetic ordering or spin freezing (spin-glass-like behaviour) (Figure S8a). Fitting to the Curie-Weiss law (between 175 K – 350 K), yields Curie Constant (C) = 0.251(1) emu K mol^{-1}, Weiss temperature (θ_{CW}) = –0.2(7) K, and χ_0 = –5.5(3) x 10^{-5} emu mol^{-1} Oe^{-1}. This Curie constant corresponds to an effective magnetic moment (μ_{eff}) of 1.416(4) $\mu_{B,}$ which is in between the expected moments for Ni^{3+} ($S=½$, μ_{eff} = 1.73 μ_B) and Ni^{4+} ($S=0$, μ_{eff} = 0 μ_B) (S-7). The Weiss temperature is significantly smaller than what might be expected from the onset of magnetic correlations around 100 K, possibly due to competing ferromagnetic (FM) and antiferromagnetic (AFM) interactions with similar magnitudes leading to a mean field θ_{CW} around zero. The magnetic susceptibility has similarities to that of pristine $NaNiO_2$, which forms a LRO state at 23 K with in-plane FM and inter-layer AFM ordering,[59,60] albeit with a significantly reduced Weiss temperature (–0.2(7) K in $Na_{2/3}NiO_2$ vs 36 K in $NaNiO_2$).[61]

DFT Calculations and AIMD Simulations

To explore the energetics of charge and cation ordering, single-point DFT calculations of the structure co-refined from X-ray and neutron diffraction data were first performed, fixing the atomic positions at the refined values. The electronic structure of the material was found to have mixed valence character with 1/3 of the Ni ions having a spin of $S(Ni_{(1)}, grey)$ = 0.47 and 2/3 of the Ni ions a spin of $S(Ni_{(2)}, blue)$ = 0.29 (Figure 2e-f)

When the atomic positions were allowed to optimise from the co-refined structure (allowing the system to change symmetry in the course of the optimisation), the structure relaxed into a lower symmetry *Pc* structure (Figure 4a). In this structure the $Ni_{(2)}$ (*4e*) site of the co-refinement structure was observed to split into $Ni_{(2A)}$ (blue) and $Ni_{(2B)}$ (light blue) (*2a*) sites. Both $Ni_{(2)}$ sites have spins of 0.29. However, only $Ni_{(2B)}$ (light blue) site is JT distorted. The $Ni_{(1)}$ site is also found to have a JT distortion, but has spin S = 0.47 The average nominal Ni charge state calculated *via* the BVS method for this model was $Ni^{3.27+}$, with $Ni_{(1)}$ (grey), $Ni_{(2A)}$ (blue) and $Ni_{(2B)}$ (light blue) sites having charges of $Ni^{3.73+}$, $Ni^{3.04+}$ and $Ni^{3.06+}$ respectively (Figure 4b). The structures obtained by DFT are compared in Figure 4 (experimental and calculated structures are all compared in S10); both the honeycomb ordering of Ni and zigzag Na vacancy ordering are retained from the combined refinement structure, in the relaxed cells. However, the relative oxidation of the $Ni_{(1)}$:$Ni_{(2)}$ sites are reversed in the two structures. The energy of this geometry-optimised structure was found to be 95 meV/atom lower than the energy of the co-refined structure without geometry optimisation (Figure 5a).

To ensure that the overall minimum-energy configuration was found, and to check that the optimisation did not converge to a local minimum in the energy landscape, AIMD simulations were performed at finite temperatures, allowing the system to overcome energy barriers on the scale of the thermal energy. At low temperatures (T < 300 K), the AIMD trajectories show undistorted NiO_6 octahedra of two different sizes and spin states, 1/3 of the octahedra being large with a spin of $S(Ni_{(1)})$ = 0.84, and 2/3 of the octahedra being small with a spin of $S(Ni_{(2)}$, blue$)$ = 0.0 (Figure 4f). The average nominal Ni charge state calculated *via* BVS method was $Ni^{3.22+}$, with $Ni_{(1)}$ (grey) and $Ni_{(2)}$ (blue) sites having charges of $Ni^{2.31+}$ and $Ni^{3.67+}$ respectively (Figure 4e). The Na ions retain the zigzag vacancy ordering throughout the AIMD run, with no Na^+ hopping observed, likely due to the relatively short timeframe (Figure 4d). No other symmetry lowering was observed, with the space group and number of Ni/Na sites preserved from the co-refined structure. The Ni-O coordination environments and spins of all models are explored in SI-8 (Figure S10).

At around room temperature, the AIMD trajectories exhibit a highly dynamic structure oscillating between the spin-disproportionated and JT-distorted states, reflective of the structure obtained *via* combined refinement of diffraction data (Figure S13). A van Vleck analysis of the AIMD trajectories (Figure S12) shows circular clusters of data points at the origin at low temperatures, confirming the undistorted nature of the spin-disproportionated octahedra.[53] With increasing temperature, the distribution of the data points becomes more triangular, illustrating a tendency of the system to become dynamically JT-elongated (equally in the 3 possible dimensions), which may be considered as phonon induced soft-JT modes.[11,62] The highest density of datapoints, however, is still centred around the pole of the van Vleck plot, *i.e.*, while there are more JT characteristics in the vibrations, the system is still mostly undistorted, stemming both from undistorted spin-disproportionated states and the high-temperature displacive phase of the JT-distorted ground state. Note that when snapshots of the dynamic trajectories at room temperature were geometry optimised (corresponding to 0 K), the snapshots relaxed to the spin-disproportionated state (Figure 4a-c). The spin-disproportionated state was found to be the overall lowest energy configuration, being 5 meV/atom more favourable than the Jahn-Teller distorted state (Figure 5a).

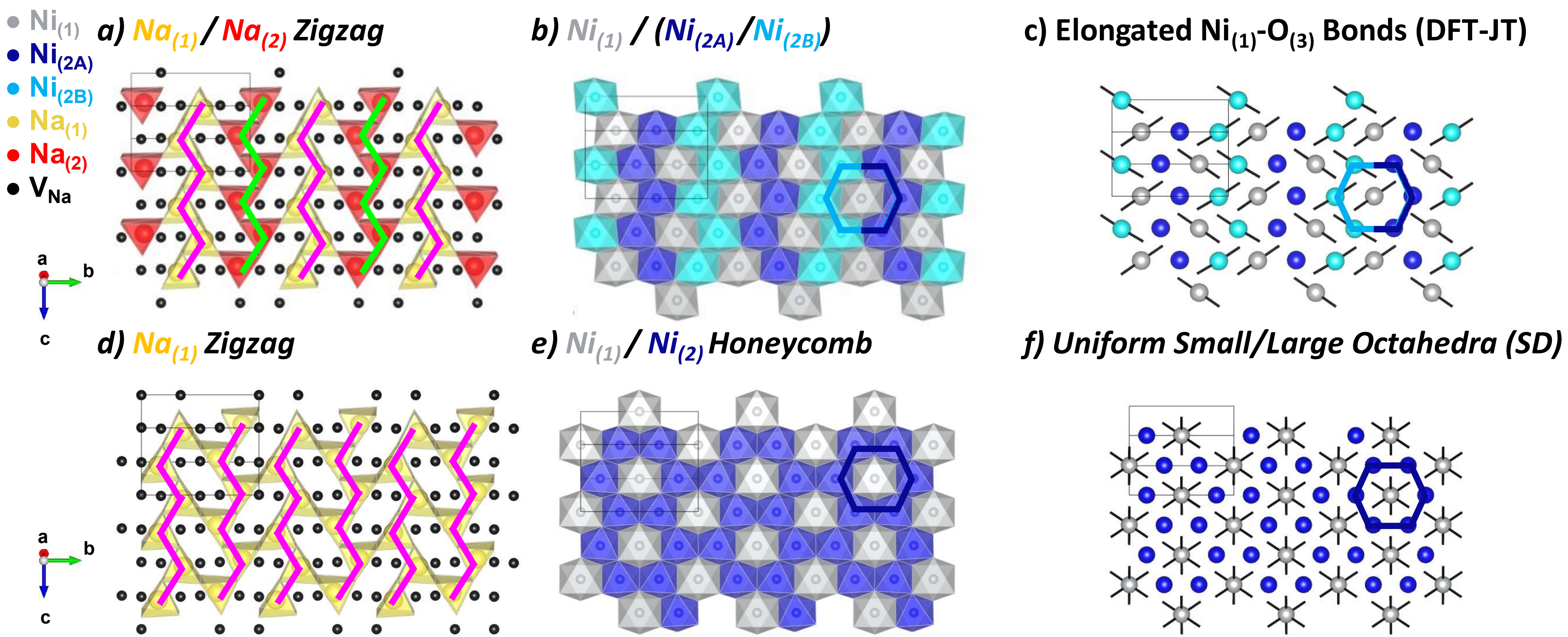

Figure 4: a-c) Jahn-Teller (DFT-JT) and d-f) spin disproportionated (SD) structural models for $P'3$ phase. a/d) Na^+/Vacancy zigzag ordering in the Na-layer (pink/green zigzags overlayed). b/e) Honeycomb (or equivalent) ordering of Ni sites on the triangular Ni lattice. Note that in the JT model, whilst there are 3 crystallographic Ni sites, $Ni_{(2A)}$/$Ni_{(2B)}$ have no difference in NiO_6 environments, thus are equivalent for the purpose of charge ordering. In a-d/d-e the unit cell (black box outline) is tiled 1x3x3 for visual clarity. c/f) Ni-O coordination within the unit cell, cutoff for long bonds drawn = 2.0 Å. In these "ball and stick" style figures, the atoms are enlarged by comparison to the figures with prisms for visual clarity.

^{23}Na NMR Fermi-contact shift calculations were performed to help distinguish between the three structures (experimental SXRD/NPD combined refinement, DFT geometry-optimisation of the experimental structure [DFT-JT], and AIMD snapshot with geometry optimisation at 0 K [Spin Disproportionation, SD]). The computed values were then compared to the observed ^{23}Na room temperature isotropic resonance at 1080 ppm. The ground-state spin-disproportionated structure is predicted to have a ^{23}Na NMR resonance at ~540 ppm (Figure 5b), whilst the DFT-JT structure is expected to exhibit resonances at 460 and 740 ppm, owing to the presence of two Na sites in this structure. Both 0 K geometry-optimised structures underestimate the shift of the experimental resonance at 1080 ppm. For the experimental structure, without geometry optimisation, a shift of 1078 ppm was predicted, in excellent agreement with the experimentally observed hyperfine shift. To validate this further, shifts were also predicted for the structure co-refined under the constraint of split O-site occupancies. The Fermi contact shifts predicted for the split-site structure are very similar to those predicted for the original experimental structure, exhibiting Fermi contact shifts at ~1040 and 1110 ppm; two separate resonances may not be resolved and they may merge to form a broad peak given the large experimental peak linewidths.

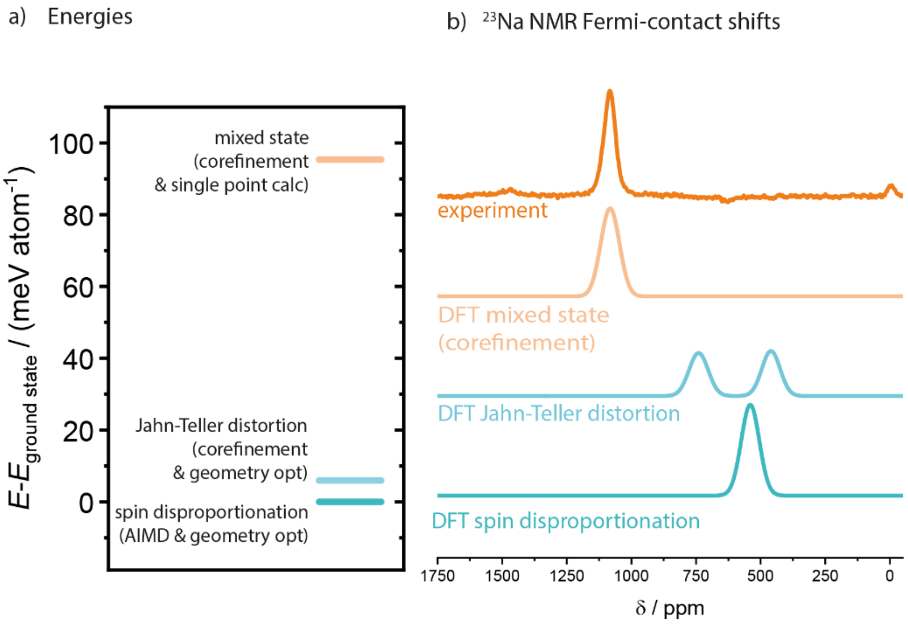

Figure 5: a) Energetics of the structural models of the $P'3$ phase shown in Figure 4 as obtained from hybrid functional DFT calculations. The energy states are labelled with their respective Na-ion ordering motifs as highlighted in Figure 4. b) Predicted ^{23}Na Fermi contact shifts for the three structural models. Both the spin-disproportionated ground state and the Jahn-Teller distorted state with a similar energy are predicted to exhibit resonances at significantly smaller shifts than the experimental spectrum. The predicted resonance of the experimental SXRD/NPD co-refined structure shows excellent agreement with the experimental spectrum.

Discussion:

The results of experimental studies and simulations give a number of possible structures for P/3 $Na_{2/3}NiO_2$. All have a honeycomb ordering of Ni charges and zigzag ordering of the Na^+ vacancies. DFT studies have predicted similar zigzag vacancy ordering as the ground state of $Na_{2/3}CrO_2$, though Na^+ is octahedrally co-ordinated (O/3) in this system.[63] However, our observed combination of honeycomb transition metal ordering and zigzag Na^+ vacancy ordering in a prismatically co-ordinated (P/3) system is also observed in the mixed transition metal compound $Na_{2/3}Cu_{1/3}Mn_{2/3}O_2$.[56] Here, the orderings are reported to minimise both intra-layer Na-Na repulsions (by preventing any high energy face-sharing Na prisms), and inter-layer repulsions by locating the occupied Na sites further from the Jahn-Teller distorted CuO_6 octahedra. We anticipate similar stabilisation of the structure in $Na_{2/3}NiO_2$, though the reduced charge difference between the Ni sites compared to Cu^{2+}/Mn^{4+} decreases the importance of this effect.

The key difference between the co-refined structure and the low energy structures obtained *via* DFT/AIMD, is the oxygen ion positions. To check that the initial refinement had not identified a local minimum, the energy-minimised structures obtained from DFT were used as starting structures in combined SXRD and NPD analysis. These starting models resulted in calculated patterns which were good visual fits to the data, including accounting for the superstructure peaks which is constant across all models (SD R_{wp} = 2.929, JT R_{wp} = 2.870). However, when the atomic coordinates were allowed to refine, the structure returned to the original structure with $Ni_{(1)}$ and $Ni_{(2)}$ with nominal charges of Ni^{3+} and $Ni^{3.5+}$ respectively. This suggests that neither of the simulated structures (JT distorted or spin-disproportionated) on their own represents a good description of the average room-temperature structure.

Magnetic measurements do not allow us to distinguish between the three structures identified. Calculating the expected effective moments (using equation ST3) for the three structures produces nearly identical values: 1.41 μ_B for the JT-distorted structure, 1.43 μ_B for the spin-disproportionated structure and 1.41 μ_B for the co-refined structure. These are all in excellent agreement with the effective moment determined from SQUID measurements (1.416[4] μ_B) (see S-7).

Whilst the ^{23}Na NMR supports the co-refined structure, as the calculated shift of this structure matches the experimental data well, its high energy (95 meV/atom above the ground state based on hybrid functional DFT calculations) relative to the spin-disproportioned ground state is sufficiently large that one would not expect it to be accessible at room temperature. Whilst kinetically stabilised phases are known to form during electrochemical deintercalation, the similarities in the three structures with only subtle changes in O ion coordination, rather than significant changes in the underlying structure, make kinetic stabilisation unlikely here. We now consider how to reconcile these results.

The two structures identified to be the lowest energy by DFT, the spin-disproportionated (SD) ground-state structure, and the lowest-energy excited state JT-distorted structure are nearly degenerate with an energy difference of only 5 meV/atom. Due to the thermal energy of the system at finite temperatures, both states are expected to be occupied and transitions between the states are expected to occur, maximising the system's entropy through a large number of possible local configurations. This fluctuating behaviour is reflected in the AIMD trajectories which, at low temperatures, mostly exhibit spin-disproportionated characteristics, with the JT contributions increasing with increasing temperature. This can be observed by visually inspecting the AIMD trajectories (Figure S12) and quantified with a van Vleck analysis of the distortion modes (SI11).[53] This analysis allows for the quantification of distortion in octahedra. The bond length distortions associated with JT distortion, are typically quantified via the Q_2 (two short, two "undistorted", and two long bonds) and Q_3 (“JT elongation”) modes. At low temperatures, the trajectories show a circular distribution of Q_2/Q_3 ordering parameters around the pole of the plot, typical of undistorted octahedra. With increasing temperature, the distribution becomes increasingly triangular resembling that of the high-temperature displacive phase of stoichiometric $NaNiO_2$ which, at room temperature, is colinearly JT-distorted.[20] This suggests that an effect of de-sodiation, is disruption of the co-operative JT distortion, similar to that of increasing temperature in the stoichiometric parent compound. The resultant phase is dynamically stabilised *via* fluctuations between a configuration with disproportionated octahedra (SD), and a configuration resembling the displacive high-temperature phase in stoichiometric $NaNiO_2$.

The question then arises of how the predicted structure at room temperature, which oscillates on the picosecond timescale between the nearly-degenerate spin-disproportionated and JT-distorted (displacive) structures, would be observed in our experiments. In both diffraction and ssNMR, a time-averaged structure of the two states would be observed. Closer inspection of the co-refined structure demonstrates features in the Ni coordination characteristic of dynamic fluctuations between the two structures. The dynamic nature of the structure is reflected in the $O_{(3)}$ positions, which can be modelled either by a split-O site, or highly anisotropic ADPs. The parent material, $NaNiO_2$, and related layered Ni^{3+} containing layered oxides typically exhibit JT-elongation. In $LiNiO_2$, AIMD simulations and experimental observations have demonstrated that the transition (reorienting the long O-Ni-O bond axes) occurs through a transition state with two long axes, and one short axis (*i.e.*, four long Ni-O bonds and two short Ni-O bonds).[12] The $Ni_{(1)}$ sites observed in the co-refined structure with two long axes and one short axis is therefore consistent with dynamic fluctuations between the spin-disproportionated and JT-distorted (displacive) structures.

Based on our combined experimental and computational study, we therefore conclude that the structure of $Na_{2/3}NiO_2$ is dynamically fluctuating between two near-degenerate states which, when time averaged, is best described by the co-refined long-range structure obtained by diffraction methods. It may be possible to experimentally explore the dynamics *via* probes such as inelastic neutron scattering, resonant inelastic x-ray scattering, or muon spin-resonance spectroscopy. However, these are beyond the scope of this study.

Charge ordering in mixed valence Ni systems is observed in $Sm_9Ni_9O_{22}$ ($SmNiO_{2.44}$) prepared from topotactic reduction of $SmNiO_3$ perovskite.[64] The reduced structure, $Sm_9Ni_9O_{22}$ contains square planar Ni^+ and Ni^{3+} in square pyramidal and octahedral coordination environments. The structure of $Na_{2/3}NiO_2$ is unique within the electrochemically produced layered transition metal $Na_{2/3}\mathit{M}O_2$ oxides. For M = V and Ti (x~0.68) both form $O'3$ phases with octahedrally coordinated Na. For M = Co, a P2 phase is experimentally observed.[21] For M = Cr an $O'3$ phase has been predicted,[65] though is yet to be reported experimentally.[66] The key features of $Na_{2/3}NiO_2$, honeycomb ordering of Ni and zigzag Na ordering, are observed in the mixed-metal $Na_{2/3}Cu_{1/3}Mn_{2/3}O_2$. We hypothesise that it is the distinct charges of the two Ni sites which stabilise the structure.

Conclusions:

We report the structure of the first de-sodiated phase of $NaNiO_2$: $Na_{2/3}NiO_2$ ($P^{/}3$), providing a framework to solve the structures of the remaining de-sodiated phases. Through the combination of experiment and simulations, the structure observed experimentally is found to be best described via time average of dynamic fluctuations between two near-degenerate states. We find that $Na_{2/3}NiO_2$ has two different Ni environments with distinct nominal charges arranged in a honeycomb ordering, with Na forming a zigzag ordering, accounting for the experimentally observed superstructure reflections. Similar structural motifs have been observed in the bi-metallic layered oxide $Na_{2/3}Cu_{1/3}Mn_{2/3}O_2$ which contains JT distorted Cu^{2+} and Mn^{4+} ions. The combined experimental and computational approach based on SXRD/NPD, ^{23}Na ssNMR spectroscopy, AIMD simulations, and DFT calculations has proven a powerful tool to characterise the complex dynamic nature of the room-temperature phase of $Na_{2/3}NiO_2$ and promises to shed light on vibrationally complex/dynamically stabilised materials, more generally. Only through a complete understanding of the parent system will it become possible to rationally design next-generation Na-ion cathode materials, through the targeted incorporation of TM dopants, to disrupt the cooperative effects of TM-orbital and Na-vacancy ordering.

References:

(1) Emsley, J. *Nature's Building Blocks: An A-Z Guide to the Elements*, Second Edition.; Oxford University Press: Oxford, New York, 2011.

(2) Xu, J.; Hu, E.; Nordlund, D.; Mehta, A.; Ehrlich, S. N.; Yang, X.-Q.; Tong, W. Understanding the Degradation Mechanism of Lithium Nickel Oxide Cathodes for Li-Ion Batteries. *ACS Appl. Mater. Interfaces* **2016**, *8* (46), 31677–31683. https://doi.org/10.1021/acsami.6b11111.

(3) Banza Lubaba Nkulu, C.; Casas, L.; Haufroid, V.; De Putter, T.; Saenen, N. D.; Kayembe-Kitenge, T.; Musa Obadia, P.; Kyanika Wa Mukoma, D.; Lunda Ilunga, J.-M.; Nawrot, T. S.; Luboya Numbi, O.; Smolders, E.; Nemery, B. Sustainability of Artisanal Mining of Cobalt in DR Congo. *Nat. Sustain.* **2018**, *1* (9), 495–504. https://doi.org/10.1038/s41893-018-0139-4.

(4) Das, H.; Urban, A.; Huang, W.; Ceder, G. First-Principles Simulation of the (Li–Ni–Vacancy)O Phase Diagram and Its Relevance for the Surface Phases in Ni-Rich Li-Ion Cathode Materials. *Chem. Mater.* **2017**, *29* (18), 7840–7851. https://doi.org/10.1021/acs.chemmater.7b02546.

(5) Genreith-Schriever, A. R.; Banerjee, H.; Menon, A. S.; Bassey, E. N.; Piper, L. F. J.; Grey, C. P.; Morris, A. J. Oxygen Hole Formation Controls Stability in $LiNiO_2$ Cathodes. *Joule* **2023**, *7* (7), 1623–1640. https://doi.org/10.1016/j.joule.2023.06.017.

(6) Barton, P. T.; Premchand, Y. D.; Chater, P. A.; Seshadri, R.; Rosseinsky, M. J. Chemical Inhomogeneity, Short-Range Order, and Magnetism in the $LiNiO_2$-NiO Solid Solution. *Chem. – Eur. J.* **2013**, *19* (43), 14521–14531. https://doi.org/10.1002/chem.201301451.

(7) An, L.; Swallow, J. E. N.; Cong, P.; Zhang, R.; Poletayev, A. D.; Björklund, E.; Didwal, P. N.; Fraser, M. W.; Jones, L. A. H.; Phelan, C. M. E.; Ramesh, N.; Harris, G.; Sahle, C. J.; Ferrer, P.; Grinter, D. C.; Bencok, P.; Hayama, S.; Islam, M. S.; House, R.; Nellist, P. D.; Green, R. J.; Nicholls, R. J.; Weatherup, R. S. Distinguishing Bulk Redox from Near-Surface Degradation in Lithium Nickel Oxide Cathodes. *Energy Environ. Sci.* **2024**, *17* (21), 8379–8391. https://doi.org/10.1039/D4EE02398F.

(8) Sicolo, S.; Sadowski, M.; Vettori, K.; Bianchini, M.; Janek, J.; Albe, K. Off-Stoichiometry, Vacancy Trapping, and Pseudo-Irreversible First-Cycle Capacity in $LiNiO_2$. *Chem. Mater.* **2024**, *36* (1), 492–500. https://doi.org/10.1021/acs.chemmater.3c02534.

(9) Dyer, L. D.; Borie, B. S. Jr.; Smith, G. P. Alkali Metal-Nickel Oxides of the Type $MNiO_2$. *J. Am. Chem. Soc.* **1954**, *76* (6), 1499–1503. https://doi.org/10.1021/ja01635a012.

(10) Chung, J.-H.; Proffen, Th.; Shamoto, S.; Ghorayeb, A. M.; Croguennec, L.; Tian, W.; Sales, B. C.; Jin, R.; Mandrus, D.; Egami, T. Local Structure of $LiNiO_2$ Studied by Neutron Diffraction. *Phys. Rev. B* **2005**, *71* (6), 064410. https://doi.org/10.1103/PhysRevB.71.064410.

(11) Radin, M. D.; Thomas, J. C.; Van der Ven, A. Order-Disorder versus Displacive Transitions in Jahn-Teller Active Layered Materials. *Phys. Rev. Mater.* **2020**, *4* (4), 043601. https://doi.org/10.1103/PhysRevMaterials.4.043601.

(12) Genreith-Schriever, A. R.; Alexiu, A.; Phillips, G. S.; Coates, C. S.; Nagle-Cocco, L. A. V.; Bocarsly, J. D.; Sayed, F. N.; Dutton, S. E.; Grey, C. P. Jahn–Teller Distortions and Phase Transitions in $LiNiO_2$: Insights from Ab Initio Molecular Dynamics and Variable-Temperature X-Ray Diffraction. *Chem. Mater.* **2024**, *36* (5), 2289–2303. https://doi.org/10.1021/acs.chemmater.3c02413.

(13) Rougier, A.; Gravereau, P.; Delmas, C. Optimization of the Composition of the $Li_{1z}Ni_1$ Electrode Materials: Structural, Magnetic, and Electrochemical Studies. *J. Electrochem. Soc.* **1996**, *143* (4), 1168. https://doi.org/10.1149/1.1836614.

(14) Genreith-Schriever, A. R.; Coates, C. S.; Märker, K.; Seymour, I. D.; Bassey, E. N.; Grey, C. P. Probing Jahn–Teller Distortions and Antisite Defects in $LiNiO_2$ with ^{7}Li NMR Spectroscopy and Density Functional Theory. *Chem. Mater.* **2024**, *36* (9), 4226–4239. https://doi.org/10.1021/acs.chemmater.3c03103.

(15) Vassilaras, P.; Ma, X.; Li, X.; Ceder, G. Electrochemical Properties of Monoclinic $NaNiO_2$. *J. Electrochem. Soc.* **2012**, *160* (2), A207. https://doi.org/10.1149/2.023302jes.

(16) Han, M. H.; Gonzalo, E.; Casas-Cabanas, M.; Rojo, T. Structural Evolution and Electrochemistry of Monoclinic $NaNiO_2$ upon the First Cycling Process. *J. Power Sources* **2014**, *258*, 266–271. https://doi.org/10.1016/j.jpowsour.2014.02.048.

(17) Wang, L.; Wang, J.; Zhang, X.; Ren, Y.; Zuo, P.; Yin, G.; Wang, J. Unravelling the Origin of Irreversible Capacity Loss in $NaNiO_2$ for High Voltage Sodium Ion Batteries. *Nano Energy* **2017**, *34*, 215–223. https://doi.org/10.1016/j.nanoen.2017.02.046.

(18) Delmas, C.; Fouassier, C.; Hagenmuller, P. Structural Classification and Properties of the Layered Oxides. *Phys. BC* **1980**, *99* (1), 81–85. https://doi.org/10.1016/0378-4363(80)90214-4.

(19) Nagle-Cocco, L. A. V.; Bull, C. L.; Ridley, C. J.; Dutton, S. E. Pressure Tuning the Jahn–Teller Transition Temperature in $NaNiO_2$. *Inorg. Chem.* **2022**, *61* (10), 4312–4321. https://doi.org/10.1021/acs.inorgchem.1c03345.

(20) Nagle-Cocco, L. A. V.; Genreith-Schriever, A. R.; Steele, J. M. A.; Tacconis, C.; Bocarsly, J. D.; Mathon, O.; Neuefeind, J. C.; Liu, J.; O'Keefe, C. A.; Goodwin, A. L.; Grey, C. P.; Evans, J. S. O.; Dutton, S. E. Displacive Jahn–Teller Transition in $NaNiO_2$. *J. Am. Chem. Soc.* **2024**. https://doi.org/10.1021/jacs.4c09922.

(21) Berthelot, R.; Carlier, D.; Delmas, C. Electrochemical Investigation of the P2–Na_xCoO_2 Phase Diagram. *Nat. Mater.* **2011**, *10* (1), 74–80. https://doi.org/10.1038/nmat2920.

(22) Meng, Y. S.; Van Der Ven, A.; Chan, M. K. Y.; Ceder, G. *Ab Initio* Study of Sodium Ordering in and Its Relation to $^{+}$ Charge Ordering. *Phys. Rev. B* **2005**, *72* (17), 172103. https://doi.org/10.1103/PhysRevB.72.172103.

(23) Braconnier, J. J.; Delmas, C.; Hagenmuller, P. Etude par desintercalation electrochimique des systemes NaxCrO2 et Na_xNiO_2. *Mater. Res. Bull.* **1982**, *17* (8), 993–1000. https://doi.org/10.1016/0025-5408(82)90124-6.

(24) Delmas, C.; Fouassier, C.; Hagenmuller, P. Structural Classification and Properties of the Layered Oxides. *Phys. BC* **1980**, *99* (1), 81–85. https://doi.org/10.1016/0378-4363(80)90214-4.

(25) Wang, L.; Wang, J.; Zhang, X.; Ren, Y.; Zuo, P.; Yin, G.; Wang, J. Unravelling the Origin of Irreversible Capacity Loss in $NaNiO_2$ for High Voltage Sodium Ion Batteries. *Nano Energy* **2017**, *34*, 215–223. https://doi.org/10.1016/j.nanoen.2017.02.046.

(26) de Boisse, B. M. Structural and Electrochemical studies of $Na_xMn_{1-y}Fe_yO_2$ and $NaNiO_2$ materials as positive electrode for Na-ion batteries. 283.

(27) Chen, X.; Wang, Y.; Wang, Y.; Dally, R. L.; Wiaderek, K.; Qiao, T.; Liu, J.; Hu, E.; Burch, K.; Lynn, J. W.; Li, X. Dynamically Preferred State with Strong Electronic Fluctuations from Electrochemical Synthesis of Sodium Manganate. *Matter* **2022**, *5* (2), 735–750. https://doi.org/10.1016/j.matt.2021.12.012.

(28) Thompson, S. P.; Parker, J. E.; Marchal, J.; Potter, J.; Birt, A.; Yuan, F.; Fearn, R. D.; Lennie, A. R.; Street, S. R.; Tang, C. C. Fast X-Ray Powder Diffraction on I11 at Diamond. *J. Synchrotron Radiat.* **2011**, *18* (4), 637–648. https://doi.org/10.1107/S0909049511013641.

(29) Chapon, L. C.; Manuel, P.; Radaelli, P. G.; Benson, C.; Perrott, L.; Ansell, S.; Rhodes, N. J.; Raspino, D.; Duxbury, D.; Spill, E.; Norris, J. Wish: The New Powder and Single Crystal Magnetic Diffractometer on the Second Target Station. *Neutron News* **2011**, *22* (2), 22–25. https://doi.org/10.1080/10448632.2011.569650.

(30) Coelho, A. A. TOPAS and TOPAS-Academic: An Optimization Program Integrating Computer Algebra and Crystallographic Objects Written in C++. *J. Appl. Crystallogr.* **2018**, *51* (1), 210–218. https://doi.org/10.1107/S1600576718000183.

(31) Rietveld, H. M. A Profile Refinement Method for Nuclear and Magnetic Structures. *J. Appl. Crystallogr.* **1969**, *2* (2), 65–71. https://doi.org/10.1107/S0021889869006558.

(32) Toraya, H. Whole-Powder-Pattern Fitting without Reference to a Structural Model: Application to X-Ray Powder Diffraction Data. *J. Appl. Crystallogr.* **1986**, *19* (6), 440–447. https://doi.org/10.1107/S0021889886088982.

(33) Campbell, B. J.; Stokes, H. T.; Tanner, D. E.; Hatch, D. M. ISODISPLACE: A Web-Based Tool for Exploring Structural Distortions. *J. Appl. Crystallogr.* **2006**, *39* (4), 607–614. https://doi.org/10.1107/S0021889806014075.

(34) Stokes, H. T.; Hatch, D. M.; Campbell, B. J. *ISODISTORT*. ISODISTORT, ISOTROPY Software Suite. iso.byu.edu.

(35) Thompson, P.; Cox, D. E.; Hastings, J. B. Rietveld Refinement of Debye–Scherrer Synchrotron X-Ray Data from Al2O3. *J. Appl. Crystallogr.* **1987**, *20* (2), 79–83. https://doi.org/10.1107/S0021889887087090.

(36) Stephens, P. W. Phenomenological Model of Anisotropic Peak Broadening in Powder Diffraction. *J. Appl. Crystallogr.* **1999**, *32* (2), 281–289. https://doi.org/10.1107/S0021889898006001.

(37) Roisnel, T.; Rodríquez-Carvajal, J. WinPLOTR: A Windows Tool for Powder Diffraction Pattern Analysis. *Mater. Sci. Forum* **2001**, *378–381*, 118–123. https://doi.org/10.4028/www.scientific.net/MSF.378-381.118.

(38) Rodríguez-Carvajal, J. Recent Advances in Magnetic Structure Determination by Neutron Powder Diffraction. *Phys. B Condens. Matter* **1993**, *192* (1), 55–69. https://doi.org/10.1016/0921-4526(93)90108-I.

(39) *ISIS Polaris Parameter Files*. https://www.isis.stfc.ac.uk/Pages/Polaris-data-analysis.aspx (accessed 2024-11-29).

(40) Hung, I.; Gan, Z. On the Magic-Angle Turning and Phase-Adjusted Spinning Sidebands Experiments. *J. Magn. Reson.* **2010**, *204* (1), 150–154. https://doi.org/10.1016/j.jmr.2010.02.004.

(41) Antzutkin, O. N.; Shekar, S. C.; Levitt, M. H. Two-Dimensional Sideband Separation in Magic-Angle-Spinning NMR. *J. Magn. Reson. A* **1995**, *115* (1), 7–19. https://doi.org/10.1006/jmra.1995.1142.

(42) Hung, I.; Zhou, L.; Pourpoint, F.; Grey, C. P.; Gan, Z. Isotropic High Field NMR Spectra of Li-Ion Battery Materials with Anisotropy >1 MHz. *J. Am. Chem. Soc.* **2012**, *134* (4), 1898–1901. https://doi.org/10.1021/ja209600m.

(43) Thurber, K. R.; Tycko, R. Measurement of Sample Temperatures under Magic-Angle Spinning from the Chemical Shift and Spin-Lattice Relaxation Rate of ^{79}Br in KBr Powder. *J. Magn. Reson.* **2009**, *196* (1), 84–87. https://doi.org/10.1016/j.jmr.2008.09.019.

(44) Perdew, J. P.; Burke, K.; Ernzerhof, M. Generalized Gradient Approximation Made Simple. *Phys. Rev. Lett.* **1996**, *77* (18), 3865–3868. https://doi.org/10.1103/PhysRevLett.77.3865.

(45) Blöchl, P. E. Projector Augmented-Wave Method. *Phys. Rev. B* **1994**, *50* (24), 17953–17979. https://doi.org/10.1103/PhysRevB.50.17953.

(46) Kresse, G.; Furthmüller, J. Efficient Iterative Schemes for Ab Initio Total-Energy Calculations Using a Plane-Wave Basis Set. *Phys. Rev. B* **1996**, *54* (16), 11169–11186. https://doi.org/10.1103/PhysRevB.54.11169.

(47) Kresse, G.; Joubert, D. From Ultrasoft Pseudopotentials to the Projector Augmented-Wave Method. *Phys. Rev. B* **1999**, *59* (3), 1758–1775. https://doi.org/10.1103/PhysRevB.59.1758.

(48) Monkhorst, H. J.; Pack, J. D. Special Points for Brillouin-Zone Integrations. *Phys. Rev. B* **1976**, *13* (12), 5188–5192. https://doi.org/10.1103/PhysRevB.13.5188.

(49) Dudarev, S. L.; Botton, G. A.; Savrasov, S. Y.; Humphreys, C. J.; Sutton, A. P. Electron-Energy-Loss Spectra and the Structural Stability of Nickel Oxide: An LSDA+U Study. *Phys. Rev. B* **1998**, *57* (3), 1505–1509. https://doi.org/10.1103/PhysRevB.57.1505.

(50) Dovesi, R.; Erba, A.; Orlando, R.; Zicovich-Wilson, C. M.; Civalleri, B.; Maschio, L.; Rérat, M.; Casassa, S.; Baima, J.; Salustro, S.; Kirtman, B. Quantum-Mechanical Condensed Matter Simulations with CRYSTAL. *WIREs Comput. Mol. Sci.* **2018**, *8* (4), e1360. https://doi.org/10.1002/wcms.1360.

(51) Vilela Oliveira, D.; Laun, J.; Peintinger, M. F.; Bredow, T. BSSE-Correction Scheme for Consistent Gaussian Basis Sets of Double- and Triple-Zeta Valence with Polarization Quality for Solid-State Calculations. *J. Comput. Chem.* **2019**, *40* (27), 2364–2376. https://doi.org/10.1002/jcc.26013.

(52) Kim, J.; Middlemiss, D. S.; Chernova, N. A.; Zhu, B. Y. X.; Masquelier, C.; Grey, C. P. Linking Local Environments and Hyperfine Shifts: A Combined Experimental and Theoretical ^{31}P and ^{7}Li Solid-State NMR Study of Paramagnetic Fe(III) Phosphates. *J. Am. Chem. Soc.* **2010**, *132* (47), 16825–16840. https://doi.org/10.1021/ja102678r.

(53) Nagle-Cocco, L. a. V.; Dutton, S. E. Van Vleck Analysis of Angularly Distorted Octahedra Using VanVleckCalculator. *J. Appl. Crystallogr.* **2024**, *57* (1), 20–33. https://doi.org/10.1107/S1600576723009925.

(54) Nagle-Cocco, L. Lnaglecocco/VanVleckCalculator, 2024. https://github.com/lnaglecocco/VanVleckCalculator (accessed 2024-12-05).

(55) Bassey, E. N.; Reeves, P. J.; Jones, M. A.; Lee, J.; Seymour, I. D.; Cibin, G.; Grey, C. P. Structural Origins of Voltage Hysteresis in the Na-Ion Cathode P2–$Na_{0.67}[Mg_{0.28}Mn_{0.72}]O_2$: A Combined Spectroscopic and Density Functional Theory Study. *Chem. Mater.* **2021**, *33* (13), 4890–4906. https://doi.org/10.1021/acs.chemmater.1c00248.

(56) Wang, X.; Yin, L.; Ronne, A.; Zhang, Y.; Hu, Z.; Tan, S.; Wang, Q.; Song, B.; Li, M.; Rong, X.; Lapidus, S.; Yang, S.; Hu, E.; Liu, J. Stabilizing Lattice Oxygen Redox in Layered Sodium Transition Metal Oxide through Spin Singlet State. *Nat. Commun.* **2023**, *14* (1), 7665. https://doi.org/10.1038/s41467-023-43031-6.

(57) Trease, N. M.; Zhou, L.; Chang, H. J.; Zhu, B. Y.; Grey, C. P. *In Situ* NMR of Lithium Ion Batteries: Bulk Susceptibility Effects and Practical Considerations. *Solid State Nucl. Magn. Reson.* **2012**, *42*, 62–70. https://doi.org/10.1016/j.ssnmr.2012.01.004.

(58) Mugiraneza, S.; Hallas, A. M. Tutorial: A Beginner's Guide to Interpreting Magnetic Susceptibility Data with the Curie-Weiss Law. *Commun. Phys.* **2022**, *5* (1), 1–12. https://doi.org/10.1038/s42005-022-00853-y.

(59) Baker, P. J.; Lancaster, T.; Blundell, S. J.; Brooks, M. L.; Hayes, W.; Prabhakaran, D.; Pratt, F. L. Thermodynamic and Magnetic Properties of the Layered Triangular Magnet $NaNiO_2$. *Phys. Rev. B* **2005**, *72* (10), 104414. https://doi.org/10.1103/PhysRevB.72.104414.

(60) Darie, C.; Bordet, P.; de Brion, S.; Holzapfel, M.; Isnard, O.; Lecchi, A.; Lorenzo, J. E.; Suard, E. Magnetic Structure of the Spin-1/2 Layer Compound $NaNiO_2$. *Eur. Phys. J. B - Condens. Matter Complex Syst.* **2005**, *43* (2), 159–162. https://doi.org/10.1140/epjb/e2005-00038-2.

(61) Holzapfel, M.; de Brion, S.; Darie, C.; Bordet, P.; Chappel, E.; Chouteau, G.; Strobel, P.; Sulpice, A.; Núñez-Regueiro, M. D. Decoupling of Orbital and Spin Degrees of Freedom in $Li_{1-x}Na_xNiO_2$. *Phys. Rev. B* **2004**, *70* (13), 132410. https://doi.org/10.1103/PhysRevB.70.132410.

(62) Srinivasan, V.; Shrivastava, K. N. A Soft Mode in the Jahn-Teller Effect. *J. Phys. C Solid State Phys.* **1979**, *12* (10), L367. https://doi.org/10.1088/0022-3719/12/10/002.

(63) Kaufman, J. L.; Van der Ven, A. First-Principles Investigation of Phase Stability in Layered Na_xCrO_2. *Phys. Rev. Mater.* **2022**, *6* (11), 115401. https://doi.org/10.1103/PhysRevMaterials.6.115401.

(64) Raji, A.; Dong, Z.; Porée, V.; Subedi, A.; Li, X.; Mundet, B.; Varbaro, L.; Domínguez, C.; Hadjimichael, M.; Feng, B.; Nicolaou, A.; Rueff, J.-P.; Li, D.; Gloter, A. Valence-Ordered Thin-Film Nickelate with Tri-Component Nickel Coordination Prepared by Topochemical Reduction. *ACS Nano* **2024**, *18* (5), 4077–4088. https://doi.org/10.1021/acsnano.3c07614.

(65) Toumar, A. J.; Ong, S. P.; Richards, W. D.; Dacek, S.; Ceder, G. Vacancy Ordering in O 3 -Type Layered Metal Oxide Sodium-Ion Battery Cathodes. *Phys. Rev. Appl.* **2015**, *4* (6), 064002. https://doi.org/10.1103/PhysRevApplied.4.064002.

(66) Jakobsen, C. L.; Andersen, B. P.; Johansen, M.; Christensen, C. K.; Drejer, A. Ø.; Karlsen, M. A.; Ravnsbæk, D. B. Structure and Evolution of Disordered Deep-Charge Phases in Na_xCrO_2 Na-Ion Battery Electrodes. *J. Power Sources* **2024**, *591*, 233875. https://doi.org/10.1016/j.jpowsour.2023.233875.

(67) Momma, K.; Izumi, F. VESTA 3 for Three-Dimensional Visualization of Crystal, Volumetric and Morphology Data. *J. Appl. Crystallogr.* **2011**, *44* (6), 1272–1276. https://doi.org/10.1107/S0021889811038970.

(68) Hunter, J. D. Matplotlib: A 2D Graphics Environment. *Comput. Sci. Eng.* **2007**, *9* (3), 90–95. https://doi.org/10.1109/MCSE.2007.55.

Acknowledgements:

J.M.A.S. acknowledges funding from the EPSRC Cambridge NanoCDT, EP/L015978/1. J.M.A.S. would like to thank the Faraday Institution NEXGENNA consortium for support as an associated PhD student. L.A.V.N−C acknowledges a scholarship EP/R513180/1 to pursue doctoral research from the UK Engineering and Physical Sciences Research Council (EPSRC) and additional funding from the Cambridge Philosophical Society. F.N.S. acknowledges funding from the Faraday Institution CATMAT project (FIRG016).

The authors acknowledge I-11 beamline at the Diamond Light Source, UK, for the synchrotron XRD measurement done under "*Cambridge BAG for new materials characterisation and structure-property relationships for a zero-carbon future*" (CY34243-2). The authors would like to thank the Science and Technologies Facilities Council for access to the ISIS facility at Harwell (experiment number: RB2410019. DOI: 10.5286/ISIS.E.RB2410019). We also thank the beamline and instrument scientists at I-11 and WISH for their continual support. Calculations were performed using the Sulis Tier 2 HPC platform hosted by the Scientific Computing Research Technology Platform at the University of Warwick (EP/T022108/1). We would like to thank George Phillips, Dr Giulio Lampronti, Dr Gheorghe-Lucian Păşcuţ, Dr Rob Armstrong and Professor Andrew Goodwin for helpful discussions. Crystal structure figures were prepared using VESTA-3,[67] plots were prepared using MatPlotLib.[68]